IEEE Robotics and Automation Letters (RA-L) paper, presented at ICRA 2026, Vienna, Austria. Cite as RA-L paper.

An Enhanced Soft Growing Robot with Mixed-Layer Jamming for Superior Load Capacity and Improved Mobility

Zheyu Li, Kui Sun, XueAi Li, Yanjiang Zou, and Hong Liu

***Abstract*—Soft robots have gained widespread attention due to their lightweight nature and inherent safety. Among them, soft growing robots (SGRs) are inspired by the growth mechanism of vines, achieving movement through tip eversion. However, their load-bearing capacity remains a significant challenge due to material limitations. The stiffness modulation approach based on layer jamming is constrained in high-curvature tip regions, preventing it from fully exhibiting its potential in unstructured environments. In this letter, motivated by enhancing the load-bearing capacity of SGR and optimizing their tip motion performance, we propose a novel mixed-layer soft growing robot (MLSGR) and introduce an innovative modification to the conventional layer jamming fabrication method. Furthermore, we establish a more accurate kinematics model and, for the first time, propose a statics model to characterize tip behavior. Experimental results demonstrate that, compared to previous work, MLSGR exhibits more than twice in load capacity, a 9% reduction in energy consumption and mechanical resistance for tip growth, a 17% improvement in tip retraction capability, and a 41.2% enhancement in kinematic model prediction accuracy (MAPE).**

***Index Terms*—Flexible structures, inflatable robot, mechanism design, soft robotics, stiffness control.**

I. Introduction

SOFT robots, due to their multi-degree-of-freedom characteristics, often outperform rigid robots in unstructured environments. This flexibility, however, introduces challenges in locomotion and manipulation [1], [2]. Soft growing robots (SGRs), inspired by vines in nature, achieve motion through tip extension while ensuring that the elongated sections do not interact with the surrounding environment. This unique locomotion strategy has garnered significant attention [3], [4], [5]. Similar eversion mechanisms have also been applied in soft inflatable fingers [6], [7], with comparable investigations into geometric and material parameters. Although SGRs present a novel approach to robotic movement, there remains a substantial research gap in their control. In many studies, actuators in soft robots are directly mapped to their controllable degrees of freedom [8], [9], [10], yet this approach increases structural and control complexity. The inherent compliance of soft robots makes them prone to unintended buckling in real-world applications, further complicating precise motion execution and stability.

Active stiffness control allows soft robots to achieve a greater number of controllable degrees of freedom without increasing the number of actuators [11]. Variable stiffness techniques enable soft robots to transition between compliant and rigid states, significantly expanding their potential applications. The commonly used stiffness modulation strategies can be broadly categorized into two groups: antagonistic mechanisms, exemplified by jamming, and direct material stiffness modulation like shape memory materials (SMMs) and low melting point materials (LMPMs). As shown in Table I, six representative variable stiffness methods with higher refinement frequently

TABLE I
Overview of Relevant Variable Stiffness Methods

Methods	Response Time	Stiffness Range	Actuation Method	Material
Granular Jamming [12], [19]	Fast (<1s)	8x~50.7x	Vacuum	Coffee/ Sand
Layer Jamming [11], [20]	Very fast (<0.5 s)	2x~5x	Vacuum	TPU/ Paper
Fiber Jamming [13], [14]	Very fast (<0.5 s)	1.4x~35x	Vacuum	PTFE/ PVC/ Nylon/ Leather
Antagonistic Method [21], [22]	N/A	2.5x~5x	Interaction	N/A
SMMs [15]-[17]	Slow (>15 s)	10x~1000x	Heat/ Electric field/ Magnetic field	Polymers/Alloys
LMPMs [18], [23]	Fast (~1 s)	10x~21.9x	Thermal conditions/ Electric power	Wax/ Polymer-s/ Alloys

Received 13 March 2025; accepted 4 July 2025. Date of publication 23 July 2025; date of current version 30 July 2025. This article was recommended for publication by Associate Editor M. Wehner and Editor Y.-L. Park upon evaluation of the reviewers' comments. This work was supported in part by the Natural Science Foundation of China under Grant 52305017 and Grant T2388101, in part by the Natural Science Foundation of Heilongjiang Province under Grant LH2023E036, in part by the State Key Laboratory of Robotics and Systems (HIT) under Grant SKLRS202501A03, in part by China Postdoctoral Science Foundation under Grant 2023M730853, in part by the Heilongjiang Postdoctoral Foundation of China under Grant LBH-Z22131, in part by the Key Research and Development Program of Heilongjiang Province under Grant 2024ZX04A01, and in part by the HIT Collaborative Innovation Center under Grant HIT-XTCX-4. *(Corresponding author: XueAi Li.)*

The authors are with the State Key Laboratory of Robotics and Systems, Harbin Institute of Technology, Harbin 150001, China (e-mail: lizzydonbelazy@163.com; xueaili@hit.edu.cn).

This article has supplementary downloadable material available at https://doi.org/10.1109/LRA.2025.3592134, provided by the authors.

Digital Object Identifier 10.1109/LRA.2025.3592134

applied in soft robotics are outlined. To facilitate comparison. Some indicators in Table I are drawn from textual data [12], [13], [14], [15], [16], [17], [18], while others are approximated from figures [11], [19], [20], [21], [22], [23].

Layer jamming occupies minimal space, is easy to fabricate, and offers a fast response time, making it a promising technique for enhancing the applicability of soft robots in exploration scenarios, including task-specific design optimization approaches for goal-oriented exploration [24]. Nevertheless, a notable limitation is that, despite efforts to exert large forces on the environment [25], load-bearing capacity has not been a primary consideration in soft growing robot research. Due to the high curvature at the tip during the extension process [20], the presence of jamming layers can severely affect the eversion dynamics of the structure.

This study aims to pave the way for the high-redundancy design of SGR prototypes, enabling it to conduct exploratory tasks under certain external disturbances while minimizing the adverse effects of variable stiffness methods on tip mobility. In this work, we propose a novel and enhanced soft growing robot, termed the mixed-layer soft growing robot (MLSGR), which combines sandpaper and printing paper layers to realize jamming-based stiffness modulation. The structural design of MLSGR deliberately partitions the main body into three distinct sections, identifying the smallest functional unit—the layer assembly. To the best of the authors' knowledge, no prior research has investigated the impact of layer jamming on SGRs from the perspective of mixed-layer structural design and modular layer-level mechanical analysis. We conducted a mechanical characterization of three different layer assemblies and determined the optimal configuration, which was subsequently validated to enhance both tip mobility and load capacity. A robot housing and a tip detection module were subsequently designed to improve the system integration of MLSGR. The fixation method of the layer assemblies was optimized, and comparative experiments were conducted to evaluate its effectiveness. The kinematic model of MLSGR was established, and, for the first time, a tip statics model under layer jamming conditions was formulated to provide theoretical support for tip mobility.

The main contributions of this paper are as follows:

1) A novel mixed-layer jamming structure combining sandpaper and printer paper, exhibiting enhanced load-bearing capacity compared to homogeneous layer structures;
2) An innovative layer fixation approach using heat-sealing techniques for enhanced tip mobility;
3) A kinematic model with improved prediction accuracy and a newly developed tip statics model accounting for layer assemblies.

II. Design

A. Soft Growing Robots Design

As shown in Fig. 1, we have designed an enhanced soft growing robot capable of three-dimensional steering, growth, and retraction while carrying a payload, with stiffness control based on layer jamming, selected for its fast response, minimal added mass, and actuation simplicity.

Fig. 1. Snapshots of MLSGR demonstrating its ability to counteract its own weight while carrying a tip-mounted sensing device in various postures.

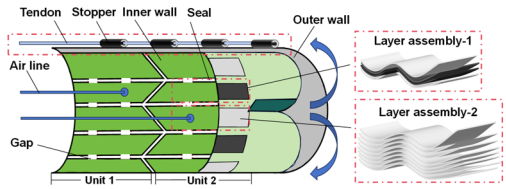

Fig. 2. A labeled cross-sectional view of the MSLGR, including two different layer assembly structures.

As pressure differences increase, the layers adhere more tightly, allowing rapid transitions between flexible and stiff state. While these previous studies have improved the manipulability of SGRs [11], [24], their contributions to load capacity enhancement remain limited. When extended to greater lengths, they compromise load-bearing capacity and increase control complexity.

Significant tip curvature changes during growth and retraction, interfering with the layer-jamming method and hindering eversion or inversion. To address this, we improved the layer-jamming method by using a mixed-layer design, combining sandpaper and printer paper. This combination was chosen because sandpaper's higher surface friction enhances stiffness when jammed, while printer paper provides flexibility in the unjammed state. This approach reduces space occupation in specific areas, enhances eversion and inversion performance, and improves load-bearing capacity.

As shown in Fig. 2, the MLSGR is divided into three main components. The first is the main body, resembling an inflatable tubular balloon, has a double-layer structure with inner and outer walls. Initially, the tip folds inward, like a rolled-up cuff. The second component is the layer assembly, located between the inner and outer walls, dividing the main body into several units. Each unit contains multiple layer assemblies of two types: Layer Assembly 1 (LA1) and Layer Assembly 2 (LA2). Due to the difference in the number of layers used, LA1—composed of a mixture of printing paper and sandpaper—has only 50% of the thickness of LA2, which is made solely of printing paper. Both the sandpaper and printing paper have a thickness of 0.1 mm per sheet. The third component is the tendon-driven unit, which enables steering of the MLSGR through tendon contraction.

According to Fig. 3, the steering principle of the MLSGR is based on adjusting the pressure differential between units. In this setup, vacuum is applied to the non-steering units, and the pressure in the steering unit is adjusted to match the pressure in the main body. As a result, the stiffness of the steering unit is minimized, allowing steering via tensile tension.

IEEE Robotics and Automation Letters (RA-L) paper, presented at ICRA 2026, Vienna, Austria. Cite as RA-L paper.

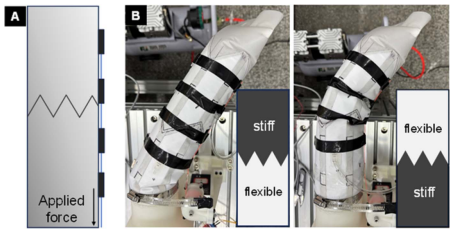

Fig. 3. Design principle of the steering method. (A) A soft growing robot is discretized into sections due to the stiffness control method. (B) Different steering effects are achieved by altering the jammed regions.

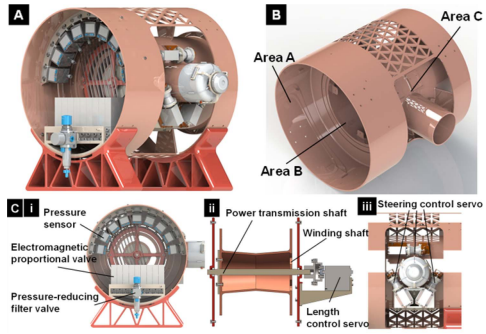

Fig. 4. 3D model of the housing and its components. (A) Isometric view of the overall MLSGR system. (B) The spatial distribution of three areas. (C) 3D models of the three sections: (i) Section A is the pneumatic control unit area, which houses various pneumatic control components; (ii) Section B, used for storing the body material of the MLSGR; (iii) Section C controls MLSGR steering with three actuators evenly spaced at 120°.

B. Robot Housing Design

This section introduces a 3D-printed airtight and multifunctional robot base made of photosensitive resin, which is functionally divided into three areas designated for the integration of electrical, pneumatic, and structural components.

Area A: Houses multiple pneumatic components, including electromagnetic proportional valves, pressure sensors, and a pressure-reducing filter valve.
Area B: an airtight area containing a servo motor serves as the length control unit.
Area C: Equipped with three drive units that apply tensile force to tendons, enabling MLSGR steering.

Fig. 4 illustrates the 3D model of the base, with the MLSGR retracted inside it, as well as the individual components of the base. The MLSGR is about 1.2 m, but its theoretical length can be much greater. The maximum length is determined by the volume of Section B, allowing a considerable length of MLSGR to be stored within a 30×40×35 cm space.

C. Tip Mount Design

SGR achieves tip motion through eversion, making the stable installation of tip devices an important area of research. The tip detection device in Fig. 5 must accommodate the conversion between the outer wall and tail materials during the arm's extension and retraction, while avoiding excessive weight that could compromise the stability of detection.

Fig. 5. Overview of tip mount design.

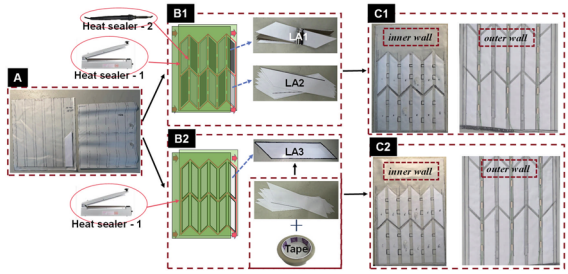

Fig. 6. Fabrication of two different dual-joint prototypes. (A) Pre-cut layers and TPU-coated 70 denier ripstop nylon. (B) MLSGR prototype (B1) uses LA1 and LA2, with the outer contours sealed by heat sealer-1 and gaps sealed by a smaller heat sealer-2. The IBR prototype (B2) utilizes LA3, secured with adhesive tape, with the outer contour sealed using heat sealer-1, while the gaps between layer assemblies remain untreated. (C) Unfolded views of the MLSGR dual-joint prototype (C1) and the IBR dual-joint prototype (C2).

The total weight of the device is less than 80 g, and it features a fastener-free fixation design where magnets provide stability. During the tip's extension and retraction, the cylindrical magnets roll relative to each other, ensuring the device remains securely fixed at the tip. The external support frame of the device is in contact with the outer wall of the inflatable arm, exposed to ambient conditions, while the internal support frame is in contact with the inner wall, located within the SGR pressurized region. Experimental results confirmed that the device can be securely installed at the tip at an extension speed of 2 cm/s and a retraction speed of 1.5 cm/s. The miniature camera, with a diameter of approximately 4.3 cm, is attached to the mounting plate of the external support frame using adhesive. The main body of the device is 3D printed from photosensitive resin.

III. Fabrication

Similar to how the design section divides the SGR into three components, the fabrication section will also prepare materials and equipment from three aspects: the MLSGR main body, layer assemblies, and tendon-driven components.

To validate the proposed robot design, two dual-joint prototypes were built: the MLSGR and the inflated beam robot (IBR), which serves as a baseline configuration adapted from previous work [11], [20]. Both prototypes have 72 total layers, with each unit containing six layer assemblies to ensure consistency. Fig. 6 illustrates the fabrication process.

Both dual-joint prototypes feature an 80 mm diameter inflatable tubing made from TPU-coated 70D ripstop nylon, a lightweight yet durable material, but their internal structures vary. The MLSGR alternates between two layer types: LA1 (4 layers of paper and P8000 sandpaper in a paper–sandpaper–sandpaper–paper sequence) and LA2 (8 layers of paper). For

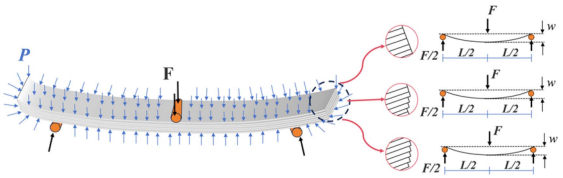

Fig. 7. The transition states of the multilayer structure from jammed to unjammed.

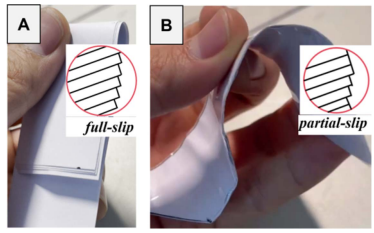

Fig. 8. The state of the layer assembly in MLSGR (A) and IBR (B) under unjammed conditions.

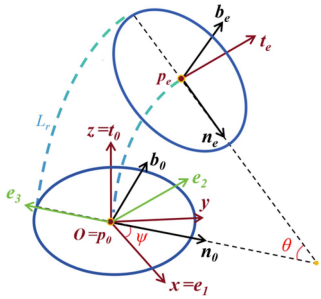

Fig. 9. A general kinematic model and coordinate frames. e_i is the unit vector from the MLSGR cross-section center to the intersection point of the i-th tendon drive module and the cross-section.

the IBR dual-joint prototype, LA3 (6 layers of paper) is used overall. To enhance load capacity, the width of each layer is set to 30 mm, with a 5 mm gap between adjacent layer assemblies. The length of each layer is 150 mm, slightly shorter than the unit length to leave room for heat-sealing gap.

An important innovation in the fabrication process is the replacement of tape-based fixation (TBF) of layer assemblies with heat-sealing fixation (HSF) (Fig. 6). Prior studies [11], [20] typically use tape and adhesive to secure layer assemblies. This method prevents the displacement of layer assemblies during movement, but a key issue is that during tip motion, the layer assemblies inevitably undergo significant deformation, generating large stresses that hinder the tip's motion and potentially cause damage to the layer assemblies. Our goal is to maintain the tip of the MLSGR compliant during extension and retraction, while ensuring that the tip can achieve high stiffness when needed. This section begins with a theoretical analysis based on layer-jamming theory [26], which defines three states: pre-slip, partial-slip, and full-slip.

As shown in Fig. 7, during the pre-slip stage, the axial shear stress between layers remains subcritical, below the static friction threshold (μP). In the partial-slip state, the outer layers behave similarly to the pre-slip state, while the internal layers experience slip. In the full-slip state, slip occurs between all layers, resembling the state of the internal layers in the partial-slip state.

The Euler-Bernoulli beam theory applies to describe the layer assembly's state [27], [28]. Under this assumption, the relationship between the central deformation w of the layer assembly and the applied force F is given by:

$$w = FL^3/48EI \tag{1}$$

where E is the Young's modulus of the layer, and L is the length of the layer, which is 150 mm in this paper.

The moment of inertia I can be expressed as:

$$I_{pre-slip} = b(nt)^3/12 \tag{2}$$

$$I_{full-slip} = bnt^3/12 \tag{3}$$

$$I_{pre-slip} < I_{partial-slip} < I_{full-slip} \tag{4}$$

where b is the width of the layer; t is the thickness of a single layer; and n is the number of layers in the layer assembly.

Fig. 8 compares the unjammed layer assemblies of the MLSGR (HSF-based) and IBR (TBF-based). The TBF layers are sealed at the edges with adhesive tape, resulting in partial constraint and limiting slip, whereas the HSF design allows freer layer movement and achieves a full-slip state. The HSF design results in a smaller moment of inertia and reduces the force required for deformation. Consequently, the tip mobility of MLSGR is theoretically superior to that of IBR.

The MLSGR is bent by applying a compressive force to the tip or one side. 3D-printed resin stoppers (15mm long, 4mm outer diameter, 1.5 mm inner diameter) guide tendons, which attach from the tip's stopper to a servo-controlled spool. By extending the dual-joint prototype along its length, the MLSGR full-arm eight-joint prototype is obtained.

IV. Modeling

A. Kinematic Model

The constant curvature assumption effectively simplifies the kinematic modeling of continuum robots by reducing infinite DOFs to a finite set [29], [30]. In the MLSGR, this assumption remains valid as stiffness modulation divided it into N segments, each maintaining constant curvature at the connections. Fig. 9 presents a general kinematic model and coordinate frames.

The Frenet-Serret formulas are applied to map configuration space to task space. At any point $\boldsymbol{p}(s)$ on the MLSGR centerline, a local coordinate system $\{\boldsymbol{p}(s) - \boldsymbol{t}(s),\ \boldsymbol{n}(s), \boldsymbol{b}(s)\}$ is defined. The initial coordinate system is $\{\boldsymbol{p}_0 - \boldsymbol{t}_0, \boldsymbol{n}_0, \boldsymbol{b}_0\} = \{\boldsymbol{p}(s) - \boldsymbol{t}(s),\ \boldsymbol{n}(s), \boldsymbol{b}(s)\}$, where $\boldsymbol{p}_0$ coincides with the origin $\boldsymbol{o}$, and $\boldsymbol{t}_0$ coincides with the $\boldsymbol{z}$-axis.

The MLSGR does not exhibit any torsional motion, so the general expression of the equation can be derived:

$$\begin{cases} d\boldsymbol{t}(s)/ds = \kappa \boldsymbol{n}(s) \\ d\boldsymbol{n}(s)/ds = -\kappa \boldsymbol{t}(s) \end{cases} \tag{5}$$

where $\kappa(s)$ represents the curvature at any point $\boldsymbol{p}(s)$ on the centerline of MLSGR.

By applying the initial conditions, the mapping of the MLSGR from the configuration space to the task space end-position vector under the constant curvature assumption is given by:

$$\boldsymbol{p}_e = \begin{bmatrix} \left(\frac{L_r}{\theta} - \frac{D_0}{2}\right) cos\psi\,(1 - cos\theta) \\ \left(\frac{L_r}{\theta} - \frac{D_0}{2}\right) sin\psi\,(1 - cos\theta) \\ \left(\frac{L_r}{\theta} - \frac{D_0}{2}\right) sin\theta \end{bmatrix} \tag{6}$$

where L_r is the maximum arc length at the intersection of the plane containing bending angle θ and the MLSGR main body. We assume that L_r is constant during the motion of MLSGR. D_0 is the diameter of the MLSGR main body.

The inverse mapping from the task space position vector to the configuration space is given by:

$$\begin{cases} \theta \;=\; arccos\left(\frac{p_z^2 - p_x^2 - p_y^2}{p_x^2 + p_y^2 + p_z^2}\right) \\ \psi \;=\; arctan2\,(p_y,\; p_x) \end{cases} \tag{7}$$

By applying the initial conditions, the complete mapping from the configuration space to the task space can be obtained:

$${}^{o}_{e}\boldsymbol{T} \;=\; \begin{bmatrix} {}^{o}_{e}\boldsymbol{R} & \boldsymbol{p}_e \\ 0^{\boldsymbol{T}} & 1 \end{bmatrix} \tag{8}$$

Mapping configuration space to actuator space helps predict MLSGR's angular displacement under different forces. The following can be derived:

$$q_i = L_r \;-\; L_i = \frac{D_0\theta}{2}\;[1 + cos\,(\psi - \gamma_i)] \tag{9}$$

where q_i is the contraction of the i-th tendon. γ_i is a parameter describing the distribution of tendons on the MLSGR, $\gamma_i = \;2\pi(i-1)/3$.

By solving for q_1, q_2, and q_3, the mapping from the actuator space to the configuration space can be obtained.

$$\begin{cases} \theta \;= 2\,(q_1 + q_2 + q_3)\,/3D_0 \\ \psi \;=\; arcsin\left[\sqrt{3}\,(q_2 - q_3)\right]/q_1 + q_2 + q_3 \end{cases} \tag{10}$$

Based on the mapping between the configuration space and the task space, the three-dimensional workspace of the eight-joint MLSGR can be derived by combining (8) and (10).

This demonstrates the utility of the kinematic model for verifying the range of motion during the design phase. The model also aids optimal design by determining multiple L_r and D_0 combinations for a given end pose, and supports feedback control by comparing real-time sensor data with predicted output to adjust tendon contraction via task, configuration, and actuator space mappings.

B. Tip Statics Model

The layer assemblies at the tip of the MLSGR undergo bending deformation, which generates a significant reaction force that is fed back to the tip. As mentioned in Section III, a force model is crucial for predicting the tip's motion.

As illustrated in Fig. 10, the MLSGR tip's axial cross-section is assumed to be a semicircle with diameter R and center at point O. A' can be expressed in terms of the bending angle θ as $A' = A \cdot (1 - cos\theta)^2/4 \;= \pi[R(1 - cos\theta)/2]^2$.

A pressure-independent offset inversion force F_I [31] remains constant during tip growth and retraction, determined

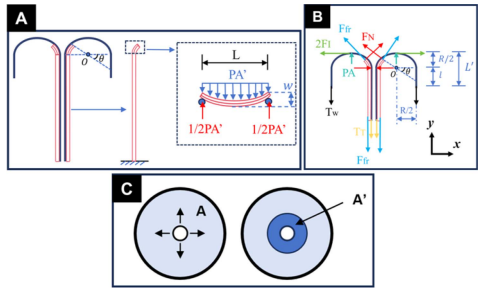

Fig. 10. The tip statics model analysis includes: (A) force analysis of the MLSGR's multilayer structure; (B) force distribution of the tip material in the XY plane; and (C) the front cross-section of the tip, where the dark blue region represents the area occupied by the layer assembly.

by materials properties. The support force F_N from internal pressure acts on the layer assembly with a magnitude of half $P \cdot A'$. Internal pressure compresses the non-everted material, generating wall friction $T_T = \mu_m \;fL'$ [32], where μ_m is the length-dependent friction coefficient and f is the normal force exerted per unit length. The everted material, fixed to the base, experiences a stabilizing force T_w. Layer friction during tip motion is $F_{fr} = \;\mu nPA'$ [33]. The everted portion of the MLSGR consists of two regions: the semicircular region at the tip with a length of $R/2$ and the extended portion l, with their sum equal to L'.

The force balance in the y-direction and the tension balance along the MLSGR body are shown as follows:

$$\begin{cases} PA + F_N \cdot sin\theta + F_{fr} \cdot cos\theta \;= T_w \;+ T_T + F_{fr} \\ 2F_I + T_w + \;F_{fr} = T_T \;+ F_{fr} \end{cases} \tag{11}$$

The expression for the deformation w is:

$$w \;= \frac{R}{2}\left(1 - cos\frac{\theta}{2}\right) = \frac{FL^3}{48EI} \tag{12}$$

By solving the above equations, the relationship between P and L' is obtained. To provide a more detailed expression, this paper discusses two cases for the layer assembly: A. Incomplete bending $(0 < \theta < \pi)$ and B. Complete bending $(\theta \geq \pi)$. We assume that when the tip length does not change, the length of the everted MLSGR is $L_{origin} = \;l + R/2$. For $0 < \theta \leq \pi/2$, $L' = L_{origin} \;+ (R/2) * sin\theta$; for $\pi/2 < \theta < \pi$, $L' = L_{origin} \;+ R - (R/2) * sin\theta$.

$$\begin{cases} \begin{cases} P \;= \frac{2\mu_m fL' - 2F_I}{A + \frac{A'}{2} sin\theta + \mu nA'(cos\theta - 1)} \\ A' = \frac{48EI\left[\frac{R}{2}\left(1 - cos\frac{\theta}{2}\right)\right]}{PL^3} \end{cases} \\ P \;= \frac{2\mu_m fL' - 2F_I + \frac{48\mu nEI}{R^2}}{\pi R^2} \end{cases} \tag{13}$$

Compared to state B, state A occurs only in a short phase of MLSGR's length change. In state B, length change is linearly related to internal pressure P, and a larger moment of inertia I requires higher P for the same elongation. This supports the hypothesis in Section III, further confirming MLSGR's superior tip motion performance.

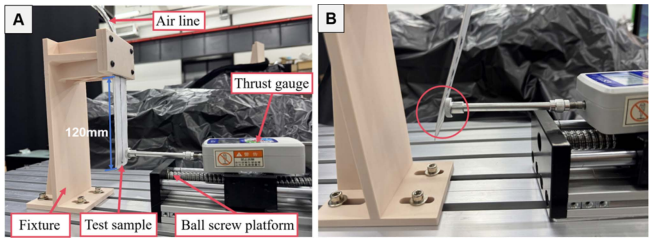

Fig. 11. (a) Experimental setup for layer group testing. (b) Layer assembly deformation under load and contact points between the gauge and layers.

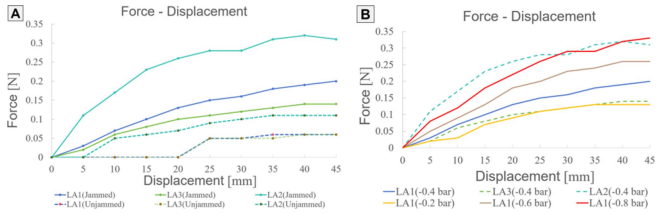

Fig. 12. Force-displacement curves. (a) Three different samples under jammed (−0.4 bar) and unjammed states (atmospheric pressure); (v) LA1 under different vacuum levels, with LA2 and LA3 serving as baselines.

V. Experiments and Results

A. Layer Assembly Testing Experiment

We built a testing platform as shown in Fig. 11 to evaluate the mechanical properties of three different layer assemblies under jammed (−0.2 bar, −0.4 bar, −0.6 bar, −0.8 bar) and unjammed (atmospheric pressure) conditions. The same TPU-coated 70D ripstop nylon used in the inflatable arm was cut to the appropriate size and formed into pouches to encase the test assemblies, with a tube inserted at one end. To enable controlled comparison, all assemblies were clamped 120 mm from the bottom using a custom fixture.

As shown in Fig. 12(a), LA1 and LA3 exhibit nearly identical stiffness when unjammed, indicating that during tip extension and retraction, their influence on the tip is similar. In contrast, LA2 demonstrates that simply increasing the thickness of homogeneous layer assemblies can result in disproportionate stiffness gains—only a one-third increase over LA3 leads to nearly double the unjammed stiffness, compromising compliance and tip mobility. In the jammed state (−0.4 bar), LA1 significantly outperforms LA3, with an average reaction force of 0.171 N compared to LA3's 0.137 N in the large deformation region (displacement >35 mm), corresponding to approximately 1.25 times that of LA3's stiffness. LA2 was incorporated into the MLSGR to improve load-bearing capacity. Fig. 12(b) illustrates that LA1's stiffness increases with vacuum level: under high vacuum, it matches LA2 in the large deformation region (>25 mm); under the low vacuum, LA1 aligns with LA3, despite being only two-thirds as thick. This highlights the potential of the mixed-layer design for stiffness enhancement.

B. MLSGR Load Capacity Experiment

Load capacity was tested by suspending different weights at a distance of 27 cm from the housing and measuring tip displacement. The same camera setup and positioning were used, with a 4 × 2 mm grid paper background to enhance visibility.

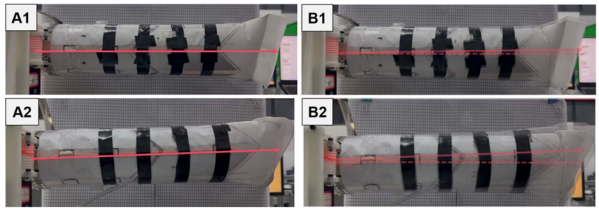

Fig. 13. (a) and (b) represent the initial and final states of MLSGR and IBR under tip-load conditions, respectively.

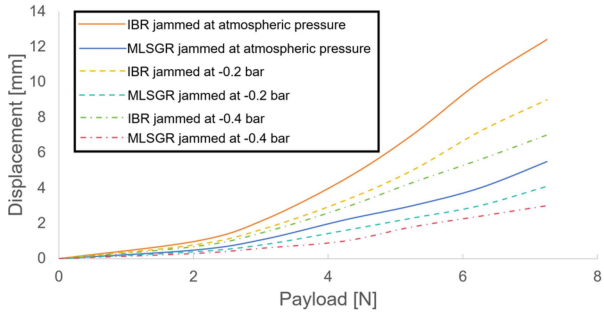

Fig. 14. Displacement-payload curves of IBR and MLSGR under different vacuum levels. A larger slope indicates lower stiffness, and MLSGR consistently demonstrates superior load capacity. In the low-load region (payload<2.5 N), the load capacities of MLSGR and IBR are similar. Load capacity rises with vacuum level, with smaller gains at higher levels.

Fig. 13 presents the states of the MLSGR and IBR under a tip load of 725 g. Notably, the tip deformation observed in the MLSGR (0.5 cm) is substantially lower than that in the IBR (1.2 cm).

Seven load sets were tested under three jamming levels with the inflatable arm internal pressure held constant at 10 kPa, as shown in Fig. 14. The MLSGR significantly outperforms the IBR in terms of load resistance, especially under higher loads, with stiffness more than twice that of the IBR when jammed at atmospheric pressure. At other vacuum levels, the MLSGR also exhibits superior load capacity.

C. MLSGR Tip Motion Experiment

Given the comparable structural dimensions and actuation durations of two prototypes, we assess eversion and retraction performance using input pressure and servo current, respectively. Lower operating pressure or servo load (current I) for a given motion length indicates reduced energy input to the system and less mechanical resistance from the layer assembly, thereby reflecting better overall performance. The growth length was set to 1 cm (5 grid cells) to monitor pressure changes, and the retraction length was set to 5 cm (25 grid cells) to obtain more current readings for averaging.

The MLSGR operates at 6.1–9.8 kPa, while the IBR requires 6.7–10.6 kPa, achieving about 9% energy savings and confirming its excellent tip motion capability. According to the tip statics model in Section IV, this lower-pressure extension persists until full eversion, highlighting MLSGR's superior tip motion.

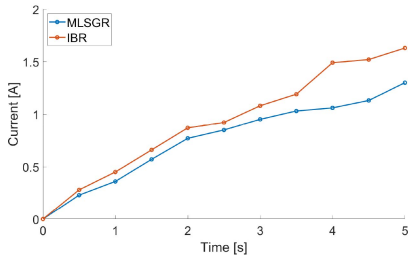

Fig. 15. Current-time curves for MLSGR and IBR in the tip retraction test.

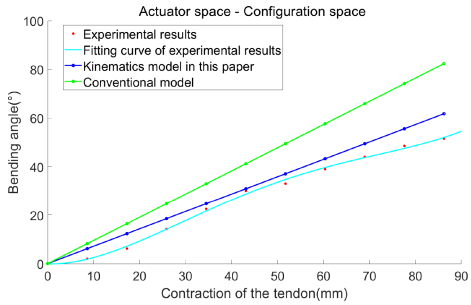

Fig. 16. Model-experiment comparison between actuator space and configuration space.

To further highlight MLSGR's superior retraction, its internal pressure (4.6 kPa) was increased by 31% over the IBR (3.5 kPa) for testing. Prior to the experiment, the vacuum generator established a vacuum pressure of −0.85 bar at the base joint within approximately 0.16 s, thereby inducing the jamming state to enhance stiffness and prevent unexpected buckling. Fig. 15 presents the current-time curves for the two prototypes. Using an Arduino-connected host computer, 10 sets of current values returned by the servo were recorded and averaged, with higher current indicating greater load. MLSGR averaged 830 mA servo current versus IBR's 1000 mA, indicating a 17% improvement in retraction performance.

D. Kinematic Model Validation Experiment

This section presents numerical simulations of the kinematic model from Section IV, as well as models based on other constant curvature assumptions [30], [34], and compares them with experimental data to validate model effectiveness.

We first experimentally validated the relationship between actuator space and configuration space in the kinematic model. During the entire experimental validation, we applied tensile force to cause bending in the dual-joint prototype. The joint at the tip is set to be in a stiff state, causing the joint near the housing to act as flexible steering joints, where wrinkles formed in this region. By adjusting the number of servo rotations, different tendon contraction amounts were achieved.

Utilizing tendon contraction and bending angle values, a comparison between the experimental and simulated mappings from actuator space to configuration space was generated, as shown in Fig. 16.

The experimental results are consistent with the simulation results. Table II presents the MAE and MAPE values for the models in this paper and conventional model. The MLSGR

TABLE II
ERROR COMPARISON (ACTUATOR-CONFIGURATION SPACE)

Models	Kinematic model in this paper	Conventional model based on the constant curvature assumption
MAPE	23.6%	64.8%
MAE	4.879	15.103

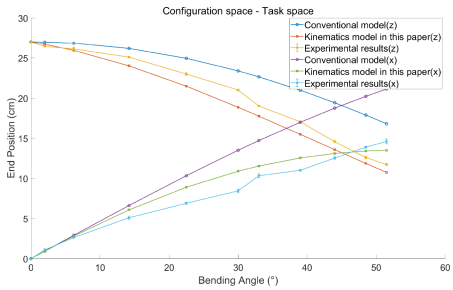

Fig. 17 Model-experiment comparison between configuration space and task space.

TABLE III
ERROR COMPARISON (CONFIGURATION-TASK SPACE)

Models	Kinematic model in this paper	Conventional model based on the constant curvature assumption
MAPE (x)	14.2%	40.1%
MAE (x)	1.065	3.993
MAPE (z)	6.5%	17.2%
MAE (z)	0.981	2.687

kinematic model has an MAE of 4.879 and a MAPE of 23.6%, while the conventional model has an MAE of 15.103 and a MAPE of 64.8%.

We extracted the tip position using a depth camera to obtain real data for the configuration space and task space. To ensure experimental continuity, we obtained the tip positions in the xz-plane and plotting the corresponding curves shown in Fig. 17.

Table III quantifies the prediction accuracy of the models in mapping from configuration space to task space. The MLSGR kinematic model achieves an MAPE of 14.2% and an MAE of 1.065 in the x-direction, whereas the conventional model has an MAPE of 40.1% and an MAE of 3.993. In the z-direction, the MLSGR kinematic model achieves an MAPE of 6.5% and an MAE of 0.981, compared to the conventional model's MAPE of 17.2% and MAE of 2.687. It is evident that the model established in this paper has better predictive capability, with a significant improvement in model accuracy.

VI. CONCLUSION AND DISCUSSION

In this letter, we present the design, fabrication, and modeling process of the Mixed-Layer Soft Growing Robot (MLSGR) and evaluate its actual performance. Based on the layer jamming theory, we incorporate a jamming layer composed of sandpaper and printer paper, combined with thicker traditional layer groups. Additionally, HSF is introduced in place of TBF to further optimize the system's performance. Experimental results demonstrate that MLSGR exhibits superior tip movement capability in the unjammed state and doubles its load-bearing capacity compared to previous designs. To enhance system integration, we

designed a base with zoning and functional attributes, along with a lightweight, unanchored tip detection device. Furthermore, the developed kinematic model exhibits higher prediction accuracy, reducing MAPE by 41.2% and MAE by 10.224. This letter also introduces a tip statics model, providing theoretical support for MLSGR's tip motion.

Although the mixed-layer assembly demonstrated superior performance, further refinement is possible by increasing the diversity of comparative configurations and investigating the effects of additional design parameters. We also plan to investigate how different substrate materials influence the mechanical behavior of SGRs, including textile, silicone and thermoplastic-based variants, to broaden the applicability of the proposed approach.

Future work will focus on optimizing trajectory planning, developing a dynamic model of MLSGR, and exploring its application in unstructured environments. We also aim to improve perception and advance teleoperation for enhanced human-robot collaboration.

REFERENCES

[1] D. Rus and M. T. Tolley, "Design, fabrication and control of soft robots," *Nature*, vol. 521, no. 7553, pp. 467–475, May 2015.

[2] O. Yasa et al., "An overview of soft robotics," *Annu. Rev. Control Robot. Auton. Syst.*, vol. 6, no. 1, pp. 1–29, May 2023.

[3] E. W. Hawkes, L. H. Blumenschein, J. D. Greer, and A. M. Okamura, "A soft robot that navigates its environment through growth," *Sci. Robot.*, vol. 2, no. 8, Jul. 2017, Art. no. eaan3028.

[4] M. M. Coad et al., "Vine robots: Design, teleoperation, and deployment for navigation and exploration," *IEEE Robot. Autom. Mag.*, vol. 27, no. 3, pp. 120–132, Sep. 2020.

[5] L. H. Blumenschein, M. M. Coad, D. A. Haggerty, A. M. Okamura, and E. W. Hawkes, "Design, modeling, control, and application of everting vine robots," *Front. Robot. AI*, vol. 7, Nov. 2020, Art. no. 548266.

[6] A. Hassan, T. Abrar, F. Aljaber, I. Vitanov, and K. Althoefer, "Eversion-capable fabric robot gripper with novel retraction mechanism," in *Proc. IEEE/RSJ Int. Conf. Intell. Robots Syst.*, 2023, pp. 10232–10237.

[7] F. Aljaber, A. Hassan, T. Abrar, I. Vitanov, and K. Althoefer, "Soft inflatable fingers: An overview of design, prototyping and sensorisation for various applications," in *Proc. IEEE Int. Conf. Soft Robot.*, 2023, pp. 1–6.

[8] R. Qi, A. Khajepour, W. W. Melek, T. L. Lam, and Y. Xu, "Design, kinematics, and control of a multijoint soft inflatable arm for human-safe interaction," *IEEE Trans. Robot.*, vol. 33, no. 3, pp. 594–609, Jun. 2017.

[9] P. Li, Y. Zhang, G. Zhang, D. Zhou, and L. Li, "A bioinspired soft robot combining the growth adaptability of vine plants with a coordinated control system," *Research*, vol. 2021, Jan. 2021, Art. no. 9843859.

[10] X. Li, H. Yue, D. Yang, K. Sun, and H. Liu, "A large-scale inflatable robotic arm toward inspecting sensitive environments: Design and performance evaluation," *IEEE Trans. Ind. Electron.*, vol. 70, no. 12, pp. 12486–12499, Dec. 2023.

[11] B. H. Do, V. Banashek, and A. M. Okamura, "Dynamically reconfigurable discrete distributed stiffness for inflated beam robots," in *Proc. IEEE Int. Conf. Robot. Automat.*, 2020, pp. 9050–9056.

[12] S. Q. An, W. H. Li, J. H. Li, H. L. Zou, and Z. C. Deng, "Tuning stiffness with granular chain structures for versatile soft robots," *Soft Robot*, vol. 10, no. 3, pp. 493–503, Jun. 2023.

[13] L. -J. Gai, J. Huang, and X. Zong, "Stiffness-tunable soft bellows actuators by cross-fiber jamming effect for robust grasping," *IEEE/ASME Trans. Mechatron.*, vol. 28, no. 5, pp. 2897–2907, Oct. 2023.

[14] L. Liow et al., "A compliant robotic leg based on fibre jamming," *IEEE Trans. Robot.*, vol. 40, pp. 4578–4597, 2024.

[15] T. P. Chenal, J. C. Case, J. Paik, and R. K. Kramer, "Variable stiffness fabrics with embedded shape memory materials for wearable applications," in *Proc. IEEE/RSJ Int. Conf. Intell. Robots Syst.*, 2014, pp. 2827–2831.

[16] Y. F. Zhang et al., "Fast-response, stiffness-tunable soft actuator by hybrid multimaterial 3D printing," *Adv. Funct. Mater.*, vol. 29, no. 15, Apr. 2019, Art. no. 1806698.

[17] M. Mattmann et al., "Thermoset shape memory polymer variable stiffness 4D robotic catheters," *Adv. Sci.*, vol. 9, no. 1, Jan. 2022, Art. no. 2103277.

[18] S. Al Harthy, S. M. H. Sadati, Z. Wu, C. A. Seneci, and C. Bergeles, "Variable stiffness soft eversion growing robot via temperature control of low-melting point alloy pressurised medium," in *Proc. Int. Symp. Med. Robot.*, 2024, pp. 1–7.

[19] H. Li, J. Sun, and J. M. Herrmann, "Beyond jamming grippers: Granular material in robotics," *Adv. Robot.*, vol. 38, no. 11, pp. 715–729, Jun. 2024.

[20] B. H. Do, S. Wu, R. R. Zhao, and A. M. Okamura, "Stiffness change for reconfiguration of inflated beam robots," *Soft Robot.*, vol. 11, no. 5, pp. 779–790, Oct. 2024.

[21] K. Suzumori, S. Wakimoto, K. Miyoshi, and K. Iwata, "Long bending rubber mechanism combined contracting and extending tluidic actuators," in *Proc. IEEE/RSJ Int. Conf. Intell. Robots Syst.*, 2013, pp. 4454–4459.

[22] S. Wang, R. Zhang, D. A. Haggerty, N. D. Naclerio, and E. W. Hawkes, "A dexterous tip-extending robot with variable-length shape-locking," in *Proc. IEEE Int. Conf. Robot. Autom.*, 2020, pp. 9035–9041.

[23] J. Lussi et al., "A submillimeter continuous variable stiffness catheter for compliance control," *Adv. Sci.*, vol. 8, no. 18, Jul. 2021, Art. no. 2101290.

[24] I. Exarchos et al., "Task-specific design optimization and fabrication for inflated-beam soft robots with growable discrete joints," in *Proc. IEEE Int. Conf. Robot. Autom.*, 2022, pp. 7145–7151.

[25] M. J. Mendoza, N. D. Naclerio, and E. W. Hawkes, "High-curvature, high-force, vine robot for inspection," in *Proc. IEEE Int. Conf. Robot. Autom.*, 2024, pp. 3014–3021.

[26] F. Caruso, G. Mantriota, L. Afferrante, and G. Reina, "A theoretical model for multi-layer jamming systems," *Mech. Mach. Theory*, vol. 172, Jun. 2022, Art. no. 104788.

[27] Y. S. Narang, J. J. Vlassak, and R. D. Howe, "Mechanically versatile soft machines through laminar jamming," *Adv. Funct. Mater.*, vol. 28, no. 17, Apr. 2018, Art. no. 1707136.

[28] R. Acevedo et al., "Characterization and modeling of layer jamming for designing engineering materials with programmable elastic-plastic behavior," *Exp. Mech.*, vol. 60, no. 9, pp. 1187–1203, Nov. 2020.

[29] M. W. Hannan and I. D. Walker, "Kinematics and the implementation of an elephant's trunk manipulator and other continuum style robots," *J. Robot. Syst.*, vol. 20, no. 2, pp. 45–63, Feb. 2003.

[30] R. J. Webster Iii and B. A. Jones, "Design and kinematic modeling of constant curvature continuum robots: A review," *Int. J. Robot. Res.*, vol. 29, no. 13, pp. 1661–1683, Nov. 2010.

[31] M. M. Coad, R. P. Thomasson, L. H. Blumenschein, N. S. Usevitch, E. W. Hawkes, and A. M. Okamura, "Retraction of soft growing robots without buckling," *IEEE Robot. Automat. Lett.*, vol. 5, no. 2, pp. 2115–2122, Apr. 2020.

[32] L. H. Blumenschein, A. M. Okamura, and E. W. Hawkes, "Modeling of bioinspired apical extension in a soft robot," in *Proc. Biomimetic Biohybrid Syst.*, M. Mangan, M. Cutkosky, A. Mura, P. Verschure, T. Prescott, and N. Lepora, Eds, 2017, pp. 522–531.

[33] Y. -J. Kim, S. Cheng, S. Kim, and K. Iagnemma, "A novel layer jamming mechanism with tunable stiffness capability for minimally invasive surgery," *IEEE Trans. Robot.*, vol. 29, no. 4, pp. 1031–1042, Aug. 2013.

[34] Z. Ying, S. Yao, J. Chen, and L. Hao, "Research on kinematics modeling of soft manipulator," in *Proc. IEEE 8th Annu. Int. Conf. CYBER Technol. Automat., Control, Intell. Syst.*, Tianjin, China, 2018, pp. 1100–1105.